

# Side Area-Assisted 3D Evaporator with Antibiofouling Function for Ultra-Efficient Solar Steam Generation

Haoxuan Li, Wei Zhu, Meng Li, Ying Li,\* Ryan T. K. Kwok, Jacky W. Y. Lam, Lei Wang, Dong Wang,\* and Ben Zhong Tang\*

Solar-driven interfacial steam generation (SISG) has been recognized as a promising strategy to solve water shortages in an eco-friendly and low-cost way. However, the practical application of SISG is vitally restricted by some inherent limits, especially for finite evaporation rate and insufficient working life of evaporator. Herein, a novel SISG system involving an all-fiber porous cylinder-like foam 3D evaporator, side area-assisted evaporation protocol, and aggregation-induced-emission-active solar absorber with “one stone two birds” function is explored. The solar absorber exhibits efficient photo-thermal conversion, endowing the side area-assisted evaporator with as high as  $3.6 \text{ kg m}^{-2} \text{ h}^{-1}$  of solar evaporation rate, which is highly desirable for SISG under 1 sun of irradiation. Moreover, the solar absorber is capable of powerfully producing reactive oxygen species upon sunlight irradiation, which results in extraordinary photodynamic killing of bacteria nearby the fiber to prevent biofouling, consequently improving the working life of evaporator.

evaporator, 3D analogues exhibit excellent evaporation performance due to the reduced light reflection and energy gaining from the environment.<sup>[9,10]</sup> For example, by increasing the height of the cylindrical cup-shaped structure, the evaporator can generate vapor with an evaporation rate of  $2.04 \text{ kg m}^{-2} \text{ h}^{-1}$  under the irradiation of 1 sun, far exceeding that for 2D structure ( $1.21 \text{ kg m}^{-2} \text{ h}^{-1}$ ).<sup>[11]</sup> Another typical 3D cone structure can achieve an evaporation rate of  $1.7 \text{ kg m}^{-2} \text{ h}^{-1}$ , 1.7 times higher than that of planar film.<sup>[12]</sup> However, majority of the previous works set the irradiation of simulated sun perpendicular to the surface of evaporator during evaporation test, while the study on simulated tilt irradiation is relatively few.<sup>[13–15]</sup> Inspired by that, side area-assisted evaporation attracted our attention for designing 3D evaporator,

## 1. Introduction

Solar-driven interfacial steam generation (SISG) is a desirable strategy to continuously produce clean water by utilizing sea water and solar energy, which both are considered as inexhaustible resources on the earth.<sup>[1–3]</sup> Of particular importance, SISG is indeed a zero-carbon emission process, making it a great potential candidate to alleviate the global water scarcity.<sup>[4,5]</sup> Over the past decades, enthusiastic efforts have been devoted by scientists on designing ideal evaporator, comprised of solar absorber for efficient light-to-heat conversion, as well as, floating structure for thermal insulation and water transportation, to increase the evaporation rate.<sup>[6–8]</sup> Compared to 2D

wherein both surface area and side area of the evaporator can absorb solar energy under natural sunlight due to its tilt irradiation function, which could consequentially amplify both effective heating area and evaporation rate. Hence, side area-assisted evaporation may offer a feasible and simple protocol to design advanced evaporators to achieve super-high evaporation rate.

The solar absorber can be categorized as plasmonic materials, carbon-based materials, and organic molecules.<sup>[16–21]</sup> Among them, plasmonic and carbon-based absorbers have their inherent weaknesses, such as, low chemical stability and high cost for plasmonic absorbers, and low stability against water and bacteria for carbon absorbers.<sup>[22–24]</sup> Besides, those developed systems generally feature a single function with transferring

H. Li, W. Zhu, M. Li, Y. Li, L. Wang, D. Wang  
Centre for AIE Research  
College of Material Science and Engineering  
Shenzhen University  
Shenzhen 518061, P. R. China  
E-mail: liyingway@szu.edu.cn; wangd@szu.edu.cn

H. Li, W. Zhu, M. Li, L. Wang  
Key Laboratory of Optoelectronic Devices and  
Systems of Ministry of Education and Guangdong Province  
College of Physics and Optoelectronic Engineering  
Shenzhen University  
Shenzhen 518061, P. R. China

 The ORCID identification number(s) for the author(s) of this article can be found under <https://doi.org/10.1002/adma.202102258>.

DOI: 10.1002/adma.202102258

H. Li  
Key Laboratory of Eco-Textiles (Ministry of Education)  
Nonwoven Technology Laboratory  
Jiangnan University  
Wuxi 214122, China

H. Li, W. Zhu, R. T. K. Kwok, J. W. Y. Lam, B. Z. Tang  
Department of Chemistry  
The Hong Kong University of Science and Technology  
Clear Water Bay, Kowloon, Hong Kong 999077, China  
E-mail: tangbenz@ust.hk

B. Z. Tang  
Shenzhen Institute of Aggregate Science and Technology  
School of Science and Engineering  
The Chinese University of Hong Kong  
Shenzhen, Guangdong 518172, China  
E-mail: tangbenz@cuhk.edu.cn

solar energy into heat, and multifunctional evaporator remain unexploited broadly but supremely desirable.<sup>[13,25]</sup> Furthermore, during evaporation, the formed warm environment around the evaporator is capable of promoting the growth of microorganisms which seriously affects working life of the evaporator, especially for wastewater treatment. Therefore, exploiting functional absorber to simultaneously achieve efficient evaporation and antibiofouling property is a major requirement.<sup>[25,26]</sup> In conventional methods, Ag,<sup>[23]</sup> ZnO<sup>[24]</sup> nanoparticles, and Mxene<sup>[27]</sup> are additionally doped into evaporator as bacteriostatic agent, endowing the evaporator with antibiofouling behavior to prevent channel plugging caused by microorganisms proliferation. Those strategies, however, require tedious labor in the preparation process and influence evaporation output due to the insufficient compatibility. Evidently, the exploration of a single material sharing both photothermal conversion and antibiofouling capacities would be an appealing yet significantly challenging task. In the circumstances, aggregation-induced-emission (AIE)-active molecule, as a newly emerged photosensitizing agent which could simultaneously afford high performing photothermal conversion and reactive oxygen species (ROS) production through rational design,<sup>[28–30]</sup> could be an

ideal candidate for constructing 3D evaporator with efficient evaporation and antibiofouling functions.

In this work, we report an all-fiber porous cylinder-like foam (AFPCF) containing AIE luminogens (AIEgens) with superior capacities of photothermal conversion and ROS generation to simultaneously realize efficient solar steam generation and antibiofouling effects (Figure 1A). Side area-assisted evaporation and antibiofouling activity are for the first time integrated into an evaporator. This presented evaporator features an interconnected porous structure with excellent hydrophilicity for vapor escaping and water supplying, side-area assisted evaporation system for increased effective evaporation area, as well as, efficient photodynamic killing of bacteria nearby the fiber to prevent biofouling, collectively offering a design blueprint for the next generation of solar steam production materials.

## 2. Results and Discussion

As shown in Figure 1A, a typical D-A-D molecule (TPA-BTDH) was well designed and facily synthesized in three steps (Figure S1, Supporting Information). In the primary step, the

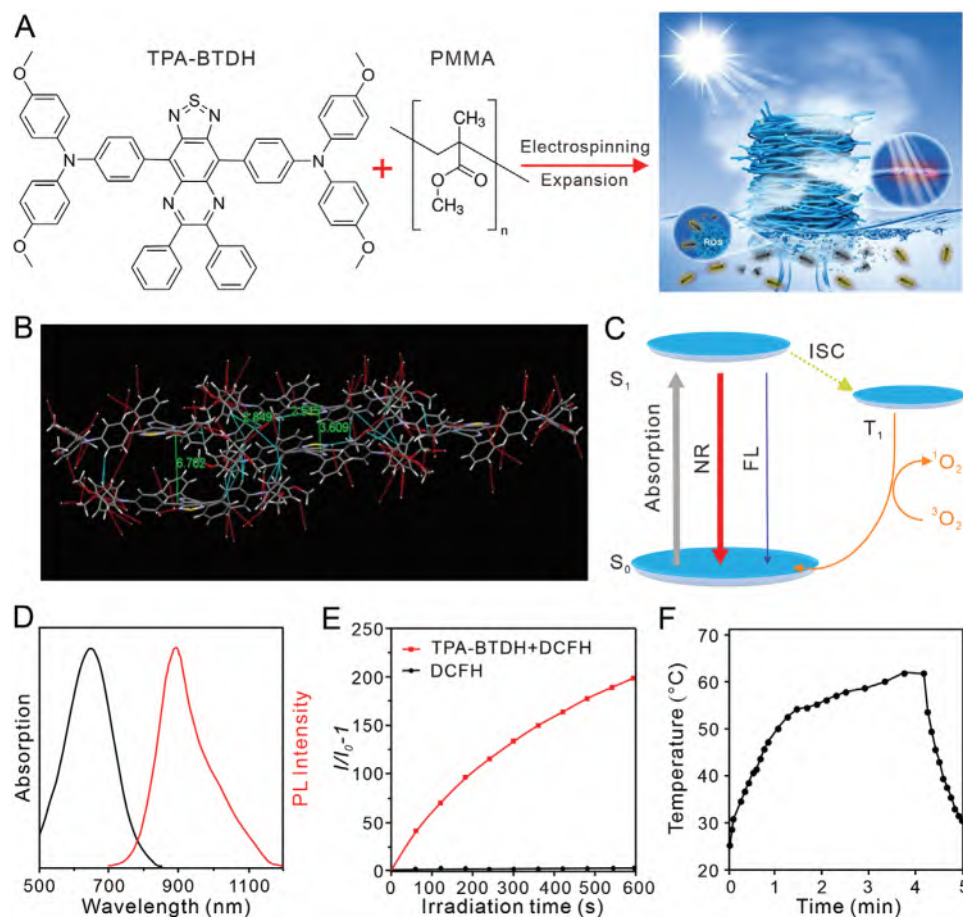


**Figure 1.** A) The structure of TPA-BTDH and a schematic for the design concept of the side area-assisted evaporator. B) The intermolecular plane distances and various intermolecular and intramolecular interactions of TPA-BTDH via single-crystal X-ray analysis. C) Jablonski diagram illustrating excited-state energy dissipations of TPA-BTDH. D) Absorption and PL spectra of TPA-BTDH in THF solution. E) ROS generation of TPA-BTDH upon xenon lamp irradiation using dichlorofluorescein (DCFH) as the indicator. F) The temperature changes of TPA-BTDH powder as it was exposed to 1 sun of irradiation.

Suzuki-Miyaura coupling reaction smoothly proceeded by employing 4-methoxy-*N*-(4-methoxyphenyl)-*N*-(4-(4,4,5,5-tetramethyl-1,3,2-dioxaborolan-2-yl)phenyl)aniline and 4,7-dibromo-5,6-dinitrobenzo[*c*][1,2,5]thiadiazole as starting materials, producing TPA-BTDNO with a yield of 53.2%. Iron-catalyzed nitro reduction of TPA-BTDNO was next conducted in the presence of acetic acid and iron powder, yielding intermediate product TPA-BTDNH. Subsequent cyclization with benzils was conducted to obtain the TPA-BTDH with a yield of 95.6%. The intermediates and final compounds are characterized by <sup>1</sup>H NMR, <sup>13</sup>C NMR, and high-resolution mass spectrum. The single crystal of TPA-BTDH was obtained in chloroform/hexane under slow evaporation. As shown in Figure 1B and Table S1, Supporting Information, the intermolecular distances between two parallel planes were as large as 3.609 and 6.702 Å, respectively, which exceeding the typical  $\pi$ - $\pi$  stacking that usually quenches the fluorescence. The twisted angles between the acceptor TQ and donor MTPA of TPA-BTDH were 51.8°, and the other dihedral angles inside the molecule were 69.71°, 72.4°, and 58.81°, respectively (Figure S2A, Supporting Information). All these features of TPA-BTDH including abundant molecular rotators, large twisted angles, and the nonplanar structure, may enable its intramolecular motions to be partially restricted but still active in fiber state, potentially allowing high photothermal conversion and ROS generation benefiting from the balanced energy dissipations (Figure 1C).

The maximum absorption wavelength of TPA-BTDH was located at 645 nm and the photoluminescence (PL) spectra of TPA-BTDH were peaked at 908 nm in the NIR-II region (Figure 1D). The strong and broad absorption is beneficial to absorb the light energy of sunlight. In addition, the long-wavelength absorption was determined to be in good accordance with the narrow HOMO-LUMO bandgap of 1.702 eV (Figure S2B, Supporting Information). Subsequently, the photosensitizing properties of TPA-BTDH were investigated in terms of ROS production and photothermal conversion. It was observed that the emission intensity of ROS indicator DCFH-DA was remarkably boosted with a 195-fold enhancement, revealing the high efficiency of ROS generation (Figure 1E). Upon solar irradiation of 1 sun, the temperature of TPA-BTDH powder increased with time and reached a maximum of 62.8°C within 150 s, suggesting its excellent capacity of transferring solar energy to heat (Figure 1F). Moreover, we evaluated the stability of TPA-BTDH against ROS. As shown in Figure S3A, Supporting Information, there is no significant change in the absorption spectra of the TPA-BTDH upon exposing to light irradiation for 24 h. In addition, as a ROS, H<sub>2</sub>O<sub>2</sub> was added into TPA-BTDH solution, and it was observed that the absorption properties of TPA-BTDH did not obviously change with or without light irradiation. These outcomes solidly suggest the excellent stability of TPA-BTDH. As comparison, the maximal absorption intensity of the commercially available photosensitizer indocyanine green (ICG) drops about 54% and 76% compared to the original value after light irradiation and light irradiation plus H<sub>2</sub>O<sub>2</sub> treatment for 24 h, respectively, indicating the much superior stability of TPA-BTDH comparing with ICG.

Encouraged by the excellent properties of TPA-BTDH, 3D-architecture nanofibrous mat with TPA-BTDH as solar absorber was then fabricated by using gas-forming expansion

technology.<sup>[20,31]</sup> First, TPA-BTDH was dipped into the fiber during electrospinning. The absorber would be stable given that TPA-BTDH was wrapped in the poly(methyl methacrylate) (PMMA) rather than coating on the matrix surface (Figure S4A,B, Supporting Information). Even though their absorption was limited in the range from 550 to 1000 nm (Figure S4C, Supporting Information), the TPA-BTDH/PMMA nanofibrous mat had over 80% of light absorption and showed considerable capacity for transferring solar to heat. The temperature of the mat could increase to 61.5 °C under 150 s of 1 sun irradiation (Figure S4D, Supporting Information). Subsequently, the TPA-BTDH/PMMA nanofibrous mats were cut into a circle with a diameter of 3 cm, treated by plasma for improving their hydrophilic, and then expanded in the NaHB<sub>4</sub> solution (1 M) for different time (Figure 2A). With the gas bubble generated and escaped through the mats (Figure 2B), the thickness changes of the nanofibrous mat following expansion were shown in Figure 2C. Evidently, the height of expanded 3D AFPCF increased from 1 to 3 and 5 cm, as the expansion time increased from 10 to 30 and 60 min, respectively. To be noted that, the hydrophilicity of the 2D nanofibrous mats given by plasma treatment before gas foaming expanding endows the 3D AFPCF with superior capability of water absorption.<sup>[31,32]</sup> Aiming to investigate the relationship between side area and evaporation rate, we prepared three groups of 3D AFPCF (diameter: 3 cm) with the height of 1, 3, and 5 cm. Their surface areas were determined to be 7 cm<sup>2</sup>, while their corresponding effective areas (surface area plus side area) were calculated to be about 10, 16, and 22 cm<sup>2</sup>, respectively (Figure 2D). The scanning electron microscope (SEM) images revealed that the gap between each layer of nanofiber increased with rising expansion time, and the thickness of layer decreased (Figure 2E and Figure S5, Supporting Information). Such an all-fiber structure bearing both interconnected pore and superior hydrophilicity endowed the 3D AFPCF with water transportation and vapor escape functions. As depicted by UV-vis-NIR absorption spectrum of the 3D AFPCF in Figure 2F, the 3D AFPCF exhibited efficient absorption in the range from 500 to 1000 nm, which is the main light energy band of natural sun, suggesting that the 3D AFPCF possesses excellent capacity to absorb sunlight. It was observed that the temperature of AFPCF in dry state rose to 59.2 °C within 10 min upon 1 sun irradiation (Figure S6, Supporting Information). In addition, the thermal conductivity of AFPCF was evaluated, and the results showed that the thermal conductivity increased from 0.0579 to 0.0605, 0.0651, and 0.0666 W m<sup>-1</sup> K<sup>-1</sup> as the temperature increased from 30 to 40, 50, and 60 °C, demonstrating a low thermal conductivity (Figure S7, Supporting Information). It seems reasonable to infer that the low thermal conductivity of AFPCF is resulted from the highly interconnected pores in the structure, and is beneficial for localized heating and further enhancing solar steam generation.<sup>[33]</sup>

To explore its solar steam generation ability, AFPCF with the height of 3 cm was wrapped by foam and then floated on a beaker filled with 3.5 wt% NaCl solution in water (Figure 3A). The temperatures of the evaporator surface and side areas were also recorded by IR camera to investigate the effect of the irradiation direction of the simulated sunlight on the evaporation capacity (Figure 3B,C). As the irradiation direction was set as

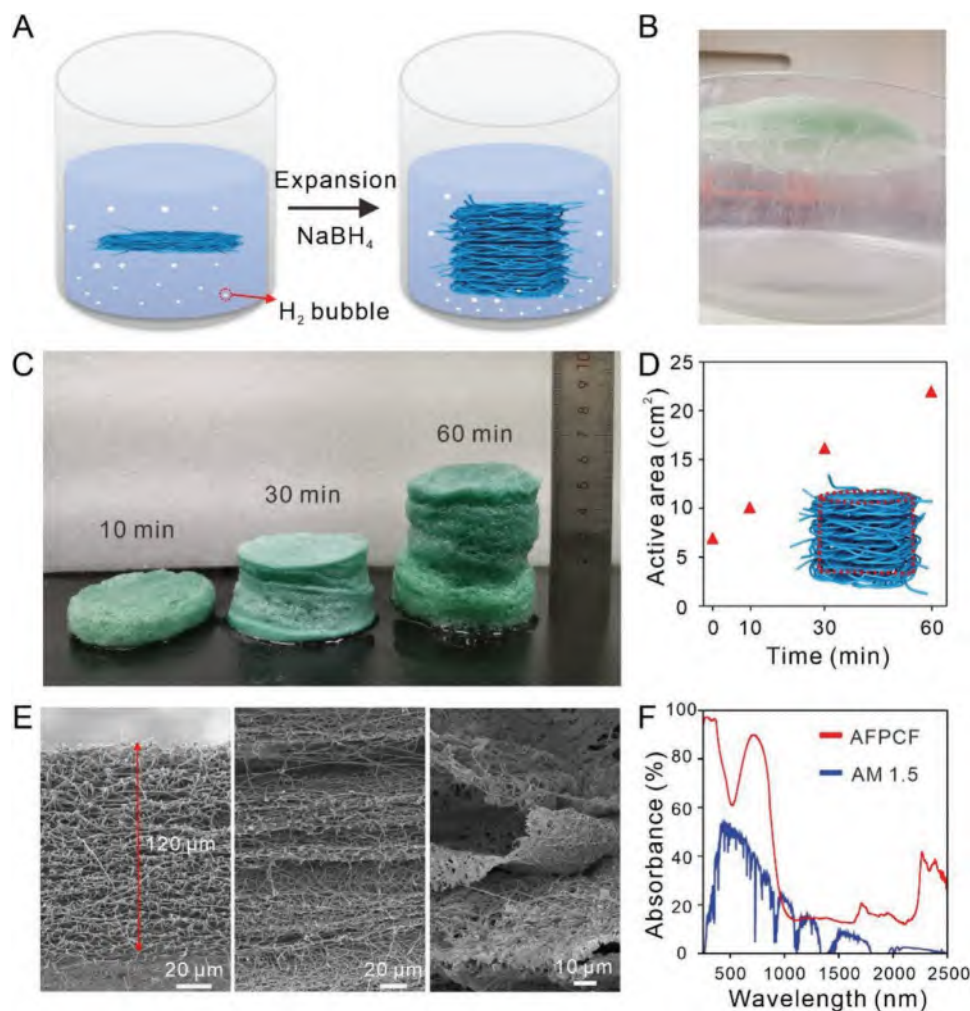


**Figure 2.** A) Schematic illustration of the expansion process from 2D nanofibrous mat to 3D structure. B) A photograph of generated bubbles as a TPA-BTDH/PMMA nanofibrous mat was placed into 1 M NaBH<sub>4</sub> solution. C) Photo image of the TPA-BTDH/PMMA nanofibrous mat after the treatment with 1 M NaBH<sub>4</sub> solution for 10, 30, and 60 min, respectively. D) The active area of AFPCF was calculated (surface area plus one side area) after the treatment with 1 M NaBH<sub>4</sub> solution for 10, 30, and 60 min, respectively. E) SEM images showing cross section morphologies of TPA-BTDH/PMMA nanofibrous mat before and after the treatment of 1 M NaBH<sub>4</sub> solution for 10 and 60 min. F) The absorption spectra of the AFPCF ranging from 250 to 2500 nm and solar spectral irradiance weighted by standard AM 1.5G solar spectrum.

vertical to the evaporator, the temperature of the evaporator surface was increased to 46.5 °C within 1 h, which was much higher than that of the evaporator side (only 28.9 °C). In addition, as the irradiation direction was tilted to the evaporator (with incident angle of 60°), the temperatures of the evaporator surface and side were increased to 44.5 and 39.5 °C within 1 h, respectively. Therefore, both surface and side of the evaporator acted as heated evaporation area to generate vapor during solar tilt irradiation. In this way, the effective evaporation area can be greatly increased without the increase of the evaporator surface. The mass of simulated seawater decreased with the increase irradiation time (Figure 3D). Under the vertical irradiation of 1 sun, the evaporation rate of the evaporator was determined to be 2.4 kg m<sup>-2</sup> h<sup>-1</sup>, and the corresponding dark evaporation rate was 0.8 kg m<sup>-2</sup> h<sup>-1</sup>. Notably, as the vertical irradiation was turned to the tilted irradiation, a dramatic increase in the evaporation rate from 2.4 to 3.6 kg m<sup>-2</sup> h<sup>-1</sup> was revealed mainly due to the additional heat generated by the side area, and the high

evaporation rate remained stable over time (Figure 3E). The incident angle of simulated sunlight was set to 180°, only side area could be irradiated, and the evaporation rate of the AFPCF decreased to 2.8 kg m<sup>-2</sup> h<sup>-1</sup> in the absence of surface evaporation (Figure S8, Supporting Information). These results indicated that side area-assisted evaporation is a facile strategy to enhance the overall evaporation based on the natural sunlight tilting irradiation.

To systematically investigate the effect of side area on the evaporation performance, the evaporators with the height of 1 and 5 cm were also tested under the vertical and tilted irradiation of 1 sun (Figure S9, Supporting Information). Under the vertical and tilted irradiation for 1 h, the surface temperature of the 1 cm-height evaporator reached at 42.2 and 41.5 °C, respectively (Figure S10, Supporting Information), while its side temperature was not recorded, since the side area was not sufficient enough to absorb solar energy. In the case of 5 cm-height evaporator, upon vertical and tilted irradiation for 1 h, the surface

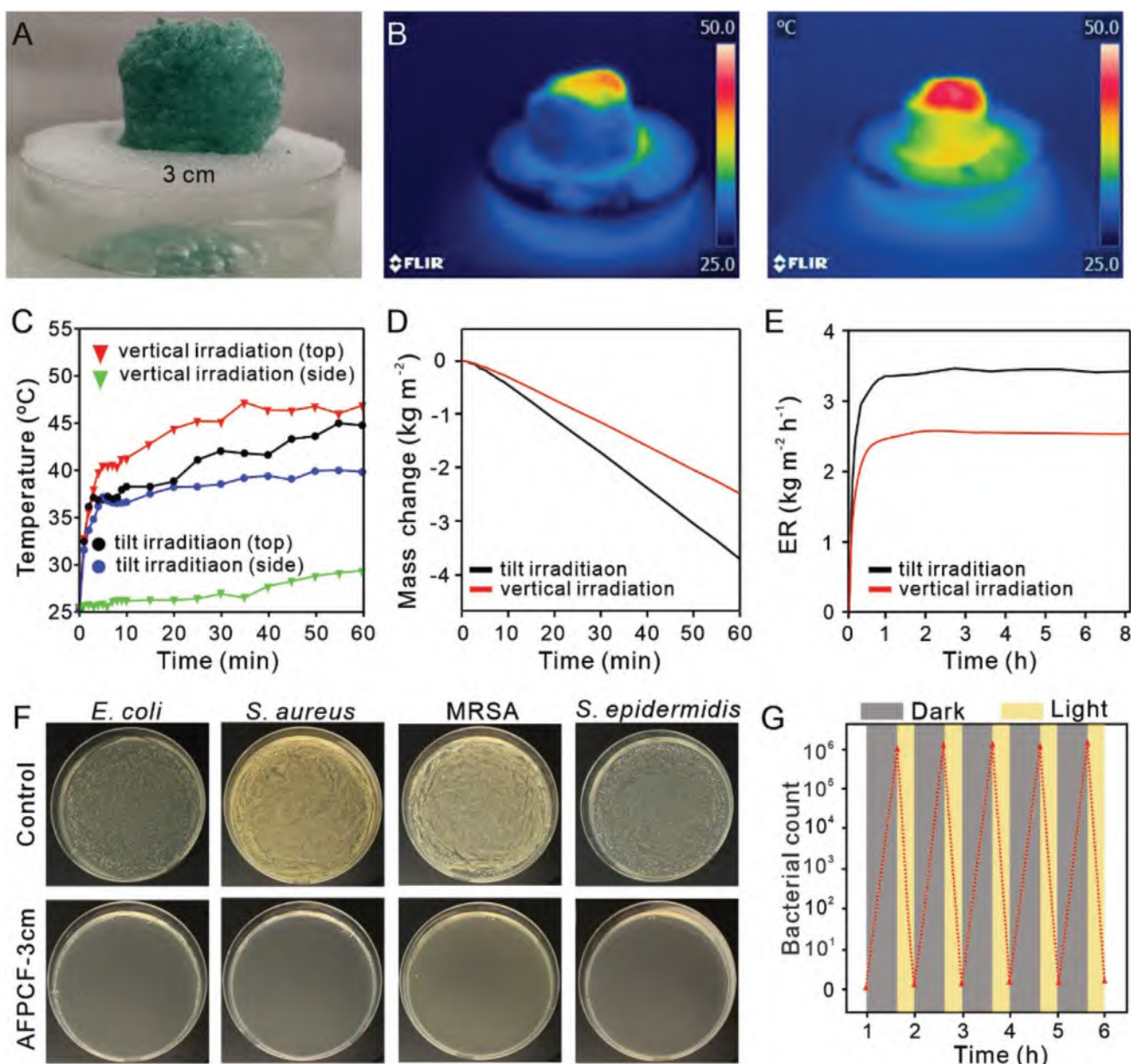


**Figure 3.** A) A photograph of AFPCF with a height of 3 cm enclosed by foam and floating on the water. B) IR thermal images showing temperature changes of the AFPCF with a height of 3 cm under vertical and tilted irradiation of 1 sun. C) A comparison between the temperature rise recorded from the surface and side of AFPCF upon the vertical and tilted irradiation of the 1 sun for 60 min. D) The mass loss of water and E) evaporation rate of AFPCF with a height of 3 cm under vertical and tilted irradiation of 1 sun for a period of time. F) Photographs of *E. coli*, *S. aureus*, MRSA, and *S. epidermidis* cultured on agar plate supplemented with TCP and AFPCF under simulated sunlight for 10 min. G) Five cycles antibacterial test of AFPCF under repeated simulated sunlight irradiation and dark condition. Each cycle,  $1 \times 10^6$  CFU mL<sup>-1</sup> *E. coli* was pipetted on the AFPCF before the dark condition.

temperatures were measured to be 43.3 and 42.5 °C, respectively, while the side temperatures were determined to be 28.2 and 36.2 °C (Figure S9C, Supporting Information). Moreover, the corresponding evaporation rates were calculated to be 1.6 and 1.8 kg m<sup>-2</sup> h<sup>-1</sup> for the 1 cm-height evaporator, and 2.8 and 3.2 kg m<sup>-2</sup> h<sup>-1</sup> for the 5 cm-height evaporator, under the vertical and tilted irradiation of 1 sun (Figure S9D,E, Supporting Information), respectively. These results indicated that the evaporation rate can be significantly enhanced by increasing the height

of the evaporator. It was also found that the evaporation rate of the 5 cm-height evaporator was lower than that of the 3 cm-height evaporator, which can be attributed to the restrained water transportation in the case of 5 cm-height evaporator. This issue could be solved by constructing a 3D smart floating structure, which can transport water to higher altitude.<sup>[10]</sup> According to classical energy efficiency calculations, all the evaporators with different side areas showed the evaporation rate beyond the theoretical limit of 2D evaporator (1.5–1.6 kg m<sup>-2</sup> h<sup>-1</sup>),<sup>[11]</sup>

which can be attributed to the additional energy harvest by the side area which absorbed the sunlight. Indeed, the presented evaporator offers a design philosophy to significantly enhance the evaporation performance.

Working life is a key criterion to estimate an evaporator. As known that a warm environment around the evaporator can be formed during the evaporation process, and promote the growth of microorganisms, which seriously affects the working life of evaporator. Inspired by the efficient ROS generation of TPA-BTDH, as well as high efficiency of bacteria photodynamic killing, the antibiofouling effect of the AFPCF was assessed by attaching four typical bacteria, *Escherichia coli*, *Staphylococcus epidermidis*, *Staphylococcus aureus*, and methicillin-resistant *S. aureus* (MRSA) on the evaporator surface, respectively. For the contact-kill test, the blank control and AFPCF samples with a diameter of 1.5 cm were loaded with 100  $\mu\text{L}$  PBS containing  $1 \times 10^7$  CFU  $\text{mL}^{-1}$  bacteria, then antibacterial assay was assessed by agar plate counting. For accuracy, six parallel samples were placed on each group. As shown in Figure 3F, four types of bacteria grow well in the blank control plate after the radiation of the simulated sunlight for 10 min. In contrast, within 10 min of irradiation, 99.86% *E. coli*, 99.91% *S. epidermidis*, 99.96% *S. aureus*, and 99.98% MRSA were killed rapidly by AFPCF, owing to its superior capability to generate ROS under visible light (Figure S11, Supporting Information). Besides, considering that the AFPCF is easy to generate ROS incessantly under the sunlight, enabling the evaporator to suppress attachment and proliferation of bacteria and/or microorganisms on the nanofiber, resulting in good antibiofouling of the evaporator. We also used *E. coli* as a model to investigate the antibacterial performance of the AFPCF on alternate day and night. Each cycle includes three stages, pipetting  $1 \times 10^6$  CFU  $\text{mL}^{-1}$  *E. coli* on the AFPCF, incubating them in dark condition for 50 min and exposing them to simulated sunlight for 10 min. Five cycles of the antibacterial result indicated that the biocidal efficacy of the AFPCF maintained consistent with a 99.9% inhibiting rate against *E. coli* (Figure 3G). Moreover, it was revealed that the AFPCF cannot generate ROS at night, due to the lack of light to drive molecule excitation, revealing the weakly antibacterial capacity in dark conditions (Figure S12, Supporting Information). This cycle test also suggested that the bacteria accumulated on the nanofiber at night can be killed in the daytime, showing excellent service life with self-antibiofouling property.

The morphological changes of bacteria on the nanofiber with or without light irradiation were visualized by SEM. Both *E. coli* and *S. aureus* exhibited rod and spherical shapes with a smooth surface in the darkness. As shown in Figure S13, Supporting Information, the cellular destruction and surface wrinkled of the *E. coli* together with the lesions of *S. aureus* were observed on the surface of the nanofiber after the AFPCF exposure to 10 min of simulated sunlight irradiation. This observation indicated that the bacteria on the nanofiber can be easily killed via disrupting bacterial cell membranes, which is similar to peroxide disinfectants. Apart from killing the bacteria attached to the nanofiber, the AFPCF can also kill the bacteria nearby the evaporator, offering a facile strategy to clean up the polluted lake and/or river. In addition, the antibacterial activity of the AFPCF under natural sunlight irradiation was also investigated. As illustrated in Figure S14, Supporting Information, each well

of the six-well plate was pipetted 5 mL PBS solution containing  $1 \times 10^7$  CFU  $\text{mL}^{-1}$  bacteria, and three groups of *E. coli*, *S. aureus*, and MRSA were tested, respectively. The AFPCF was placed on three wells, and the other three wells were set as blank control. Under the irradiation of natural sunlight with  $0.76 \text{ kW m}^{-2}$  for 1 h (2:00 PM to 3:00 PM), viable colonies of *E. coli*, *S. aureus*, and MRSA grew well on the plates in the absence of AFPCF, whereas a significant decrease in all types of bacteria survival occurred in the presence of AFPCF. Owing to the excellent insulation performance of the AFPCF, there are no significant changes in temperature of PBS solution with or without AFPCF under the irradiation of sunlight. Hence, ROS played a key role in killing bacteria. Limited by the operating distance of ROS, only the bacteria near the evaporator can be efficiently killed, which is beneficial to treat surface water pollution without affecting fish or other organisms living in deep water.

To explore the water purification capacity of the AFPCF, two samples including simulated seawater with five primary ions ( $\text{Na}^+$ ,  $\text{Mg}^{2+}$ ,  $\text{K}^+$ ,  $\text{Ca}^{2+}$ , and  $\text{Pb}^{2+}$ ) and waste water with four types of bacteria (*E. coli*, *S. epidermidis*, *S. aureus*, MRSA) were carefully prepared. In order to collect purified water from the samples, we also hand-made a closed evaporation system, which consists of a glass cover with high transmittance, a Dewar flask filled with sample water and the evaporator (Figure 4A). We first used the simulated seawater to conduct the test, as the evaporation system under the tilted irradiation of 1 sun, vapor generated and condensed on the inner wall of the glass cover (Figure S15A, Supporting Information). With the increase of the irradiation time, the vapor became liquid and formed droplets, and then merged together (Figure 4B), and the humidity of inner glass cover increased from 60% to 99% within 1 h of irradiation (Figure S15B, Supporting Information). After purification by the solar driven evaporation system, the light yellow-colored simulated seawater was transferred into a colorless and clear liquid (Figure S16A, Supporting Information). As noted by inductively coupled plasma mass spectrometry, the concentration of ions ( $\text{Na}^+$ ,  $\text{Mg}^{2+}$ ,  $\text{K}^+$ ,  $\text{Ca}^{2+}$ , and  $\text{Pb}^{2+}$ ) in the simulated seawater decreased from  $10^3$  to  $10^{-1} \text{ mg L}^{-1}$  with an efficiency of 99.9% after solar evaporation treatment, which was much lower than the World Health Organization (WHO) standard for drinking water (1‰) (Figure 4C).<sup>[34]</sup> Importantly, the presented evaporator can continue to generate clean water stably during 7 days cycles (8 h per day), indicating its excellent durability and superior salt-resisting performance in solar desalination (Figure S16B, Supporting Information). Apart from ions pollutants, bacteria and microorganism pollution is another challenge for water purification. We then utilized the evaporation system to purify the waste water containing four types of bacteria. As shown in Figure 4D,E, there is no bacterial clone could be observed in the condensed water, showing the efficient removal of the bacteria. These results strongly suggested that this developed AFPCF evaporator was capable of achieving water purification from seawater and waste water via solar irradiation.

### 3. Conclusion

An advanced 3D evaporator, namely AFPCF, that combines side area-assisted evaporation with a “one-stone two-birds”

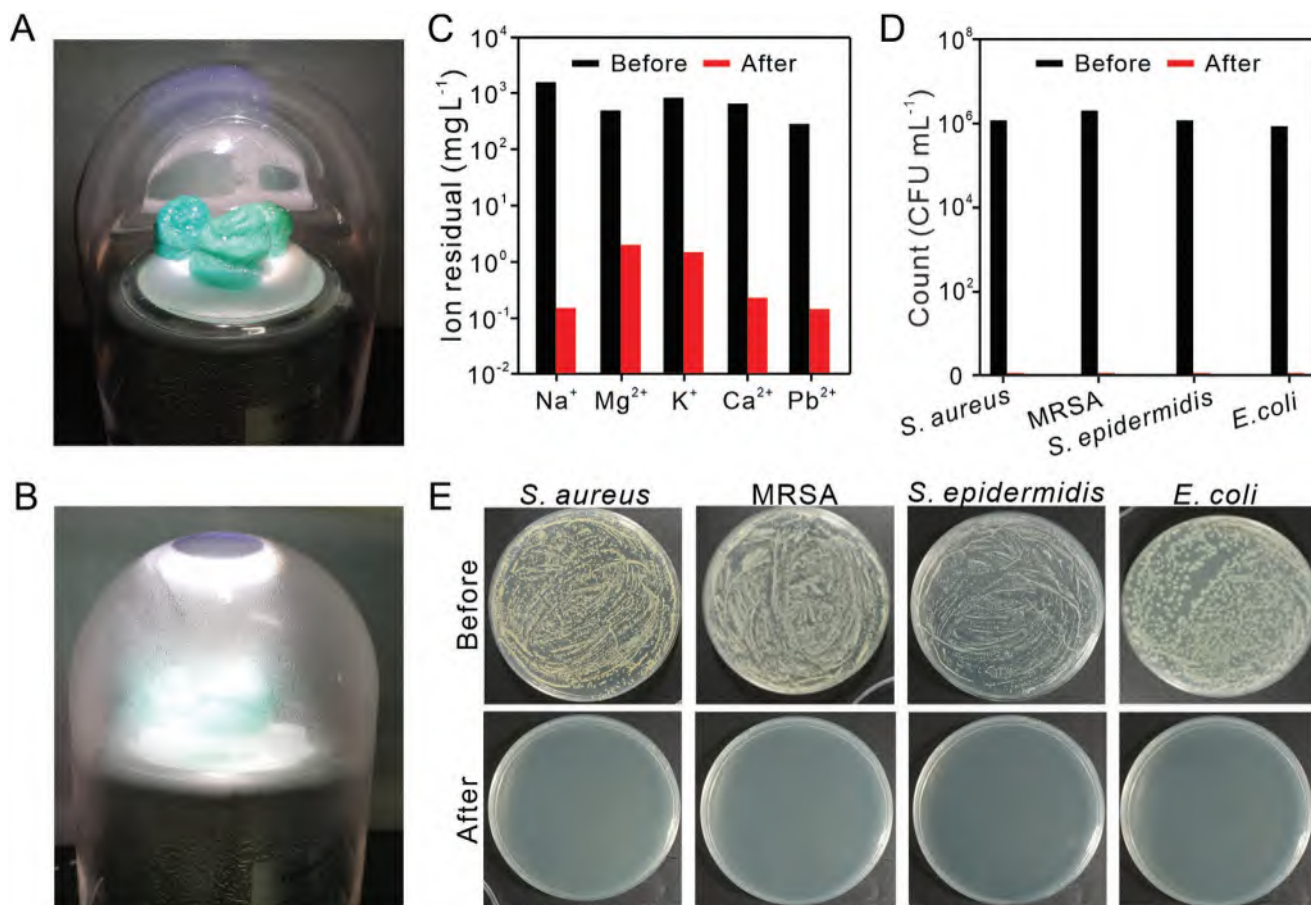


**Figure 4.** A) A photograph of the hand-made solar steam generation device containing a glass cover, an AFPCF evaporator, and a Dewar flask filled with seawater or waste water. B) A photograph showing clean water condensed on the inner wall of the glass cover. C) The concentrations of ions (Na<sup>+</sup>, Mg<sup>2+</sup>, K<sup>+</sup>, Ca<sup>2+</sup>, and Pb<sup>2+</sup>) in the simulated seawater and the collected clean water after evaporation. D) The counts of bacterial clones in the simulated wastewater and the collected water after evaporation ( $n = 3$ ). E) Photographs of *S. aureus*, MRSA, *S. epidermidis*, and *E. coli* cultured on agar plate, where from wastewater and the collected water after evaporation.

AI Egen is developed to realize excellent evaporation property and antibiofouling performance. AFPCF evaporator exhibits interconnected pore and large side area, which are beneficial for vapor escaping and gaining energy from tilted sunlight irradiation. The presence of the tactfully designed AI Egen endows the evaporator with excellent photothermal conversion and photodynamic antibacterial capacity. Notably, solar evaporation rate of the evaporator is determined to be as high as  $3.6 \text{ kg m}^{-2} \text{ h}^{-1}$ , which is highly desirable for SISG under 1 sun of irradiation. Moreover, the continuous ROS generation of the AI Egen under the irradiation of sunlight highly inhibits the growth of bacteria nearby the evaporator, revealing the superior antibiofouling performance. The presented evaporator is further used to purify simulated seawater and waste water containing various bacteria, and achieved a high-quality purification meeting the WHO standards for drinking water. Therefore, the multifunctional side area-assisted evaporator opened a window to construct next generation of smart evaporator for water purification and other applications, including moisture management, marine ecosystem, and wastewater treatment.

## Supporting Information

Supporting Information is available from the Wiley Online Library or from the author.

## Acknowledgements

H.L. and W.Z. contributed equally to this work. This work was partially supported by the Natural Science Foundation for Distinguished Young Scholars of Guangdong Province (2020B1515020011), the National Natural Science Foundation of China (21801169, 22005195), the Science and Technology Foundation of Shenzhen City (JCYJ20190808153415062, RCYX20200714114525101), and China Postdoctoral Science Foundation (2020M672797). The authors would also like to thank Instrumental Analysis Center of Shenzhen University for SEM analysis.

## Conflict of Interest

The authors declare no conflict of interest.

## Data Availability Statement

The data that support the findings of this study are available from the corresponding author upon reasonable request.

## Keywords

aggregation-induced emission, antifouling, nanofiber, side area assisted evaporation, solar steam generation

Received: March 23, 2021

Revised: April 30, 2021

Published online: July 26, 2021

- 
- [1] P. Tao, G. Ni, C. Song, W. Shang, J. Wu, J. Zhu, G. Chen, T. Deng, *Nat. Energy* **2018**, *3*, 1031.
- [2] F. Zhao, Y. Guo, X. Zhou, W. Shi, G. Yu, *Nat. Rev. Mater.* **2020**, *5*, 388.
- [3] M. Gao, L. Zhu, C. K. Peh, G. W. Ho, *Energy Environ. Sci.* **2019**, *12*, 841.
- [4] L. Zhou, X. Li, G. W. Ni, S. Zhu, J. Zhu, *Natl. Sci. Rev.* **2019**, *6*, 562.
- [5] Y. Guo, H. Lu, F. Zhao, X. Zhou, W. Shi, G. Yu, *Adv. Mater.* **2020**, *32*, 1907061.
- [6] Y. Pang, J. Zhang, R. Ma, Z. Qu, W. Lee, T. Luo, *ACS Energy Lett.* **2020**, *5*, 437.
- [7] J. Zhou, Y. Gu, P. Liu, P. Wang, L. Miao, J. Liu, A. Wei, X. Mu, J. Li, J. Zhu, *Adv. Funct. Mater.* **2019**, *50*, 1903255.
- [8] Y. S. Jun, X. Wu, D. Ghim, Q. Jiang, S. Cao, S. Singamaneni, *Acc. Chem. Res.* **2019**, *52*, 1215.
- [9] N. Xu, X. Hu, W. Wu, X. Li, L. Zhou, S. Zhu, J. Zhu, *Adv. Mater.* **2017**, *29*, 1606762.
- [10] X. Xu, T. Gao, C. Han, J. Xu, G. Owens, H. Xu, *Sci. Bull.* **2019**, *64*, 1625.
- [11] Y. Shi, R. Li, Y. Jin, S. Zhuo, L. Shi, J. Chang, S. Hong, K. C. Ng, P. Wang, *Joule* **2018**, *2*, 1171.
- [12] Y. Wang, C. Wang, X. Song, M. Huang, S. K. Megarajan, S. F. Shaikat, H. Jiang, *J. Mater. Chem. A* **2018**, *6*, 9874.
- [13] S. L. Wu, H. Chen, H. L. Wang, X. Chen, H. C. Yang, S. B. Darling, *Environ. Sci.: Water Res. Technol.* **2021**, *7*, 24.
- [14] X. Xu, Z. Wu, Y. Wang, T. Gao, Q. Li, H. Xu, *Adv. Sci.* **2021**, *8*, 2002501.
- [15] X. Mu, Y. Gu, P. Wang, A. Wei, Y. Tian, J. Zhou, Y. Chen, J. Zhang, Z. Sun, J. Liu, L. Sun, S. Tanemuura, L. Miao, *Sol. Energy Mater. Sol. Cells* **2021**, *220*, 110842.
- [16] N. Xu, J. Li, Y. Wang, C. Fang, X. Li, Y. Wang, L. Zhou, B. Zhu, Z. Wu, S. Zhu, J. Zhu, *Sci. Adv.* **2019**, *5*, eaaw7013.
- [17] L. Zhou, Y. Tan, J. Wang, W. Xu, Y. Yuan, W. Cai, S. Zhu, J. Zhu, *Nat. Photonics* **2016**, *10*, 393.
- [18] X. Dong, L. Cao, Y. Si, B. Ding, H. Deng, *Adv. Mater.* **2020**, *32*, 1908269.
- [19] Y. Kuang, C. Chen, S. He, E. M. Hitz, Y. Wang, W. Gan, R. Mi, L. Hu, *Adv. Mater.* **2019**, *31*, 1900498.
- [20] H. Li, H. Wen, Z. Zhang, N. Song, R. T. K. Kowk, J. W. Y. Lam, L. Wang, D. Wang, B. Z. Tang, *Angew. Chem., Int. Ed.* **2020**, *59*, 20371.
- [21] H. Li, H. Wen, J. Li, J. Huang, D. Wang, B. Z. Tang, *ACS Appl. Mater. Interfaces* **2020**, *12*, 26033.
- [22] C. Liu, K. Hong, X. Sun, A. Natan, P. Luan, Y. Yang, H. Zhu, *J. Mater. Chem. A* **2020**, *8*, 12323.
- [23] Y. Xu, J. Ma, Y. Han, H. Xu, Y. Wang, D. Qi, W. Wang, *Chem. Eng. J.* **2020**, *384*, 123379.
- [24] X. Y. Wang, J. Xue, C. Ma, T. He, H. Qian, B. Wang, J. Liu, Y. Lu, *J. Mater. Chem. A* **2019**, *7*, 16696.
- [25] C. Chen, Y. Kuang, L. Hu, *Joule* **2020**, *3*, 683.
- [26] V. D. Dao, N. H. Vu, S. Yun, *Nano Energy* **2020**, *68*, 104324.
- [27] X. J. Zha, X. Zhao, J. H. Pu, L. S. Tang, K. Ke, R. Y. Bao, L. Bai, Z. Y. Liu, M. B. Yang, W. Yang, *ACS Appl. Mater. Interfaces* **2019**, *11*, 36589.
- [28] M. Kang, Z. Zhang, N. Song, M. Li, P. Sun, X. Chen, D. Wang, B. Z. Tang, *Aggregate* **2020**, *1*, 80.
- [29] W. Xu, M. M. S. Lee, J. J. Nie, Z. Zhang, R. T. K. Kwok, J. W. Y. Lam, F. J. Xu, D. Wang, B. Z. Tang, *Angew. Chem., Int. Ed.* **2020**, *59*, 9610.
- [30] Z. Zhang, W. Xu, M. Kang, H. Wen, H. Guo, P. Zhang, L. Xi, L. Wang, D. Wang, B. Z. Tang, *Adv. Mater.* **2020**, *32*, 2003210.
- [31] S. Chen, J. V. John, A. McCarthy, M. A. Carlson, X. Li, J. Xie, *Appl. Phys. Rev.* **2020**, *7*, 021406.
- [32] J. Jiang, M. A. Carlson, M. J. Teusink, H. Wang, M. R. MacEwan, J. Xie, *ACS Biomater. Sci. Eng.* **2015**, *1*, 991.
- [33] G. Ni, G. Li, S. V. Boriskina, H. Li, W. Yang, T. Zhang, G. Chen, *Nat. Energy* **2016**, *1*, 16126.
- [34] F. Edition, *WHO Chron.* **2011**, *38*, 104.